



Significance of Cu-Fe₃O₄ on fractional Maxwell fluid flow over a cone with Newtonian heating

Hanifa Hanif, Arshad Khan, Mohd Rijal Illias & Sharidan Shafie

To cite this article: Hanifa Hanif, Arshad Khan, Mohd Rijal Illias & Sharidan Shafie (2024) Significance of Cu-Fe₃O₄ on fractional Maxwell fluid flow over a cone with Newtonian heating, Journal of Taibah University for Science, 18:1, 2285491, DOI: [10.1080/16583655.2023.2285491](https://doi.org/10.1080/16583655.2023.2285491)

To link to this article: <https://doi.org/10.1080/16583655.2023.2285491>



© 2023 The Author(s). Published by Informa UK Limited, trading as Taylor & Francis Group.



View supplementary material [↗](#)



Published online: 08 Dec 2023.



Submit your article to this journal [↗](#)



Article views: 639



View related articles [↗](#)



View Crossmark data [↗](#)



Citing articles: 1 View citing articles [↗](#)

Significance of Cu-Fe₃O₄ on fractional Maxwell fluid flow over a cone with Newtonian heating

Hanifa Hanif^{a,b}, Arshad Khan^c, Mohd Rijal Illias^d and Sharidan Shafie^b

^aDepartment of Mathematics, Sardar Bahadur Khan Women's University, Quetta, Pakistan; ^bDepartment of Mathematical Sciences, Faculty of Science, Universiti Teknologi Malaysia, Johor Bahru, Johor, Malaysia; ^cInstitute of Computer Sciences and Information Technology, The University of Agriculture, Peshawar, Pakistan; ^dFaculty of Computer and Mathematical Sciences, Universiti Teknologi MARA, Shah Alam, Selangor, Malaysia

ABSTRACT

The goal of this research is to investigate fractional Maxwell hybrid nanofluids utilizing partial differential equations in terms of Caputo time fractional derivatives. Specifically, the effect of Newtonian heating on the thermal performance of a fractional Maxwell hybrid nanofluid moving over a permeable cone in the presence of thermal radiation and heat generation is considered. The Crank–Nicolson method and L1 algorithm of Caputo derivative are used to find numerical solutions to the considered nonlinear problem. The effects of significant flow factors on fluid properties are examined and illustrated in various graphs. According to the results, the thermal performance of the fluid raised by 0.4%, 6.1%, and 3.1% on adding 4% volume fraction of Fe₃O₄, Cu, and Cu – Fe₃O₄, respectively, in the base fluid.

ARTICLE HISTORY

Received 11 July 2023
Revised 30 October 2023
Accepted 15 November 2023

KEYWORDS

Nanofluid; Maxwell fluid model; fractional derivative; finite difference method

Nomenclature

Roman letters



(u, v)	velocity components (ms^{-1})
$C_1 - C_5$	nanofluid constants
C_f	Skin friction
C_p	specific heat capacity ($\text{Jkg}^{-1}\text{K}^{-1}$)
g	gravitational acceleration (ms^{-2})
Gr	Grashof number
K	non-dimensional porosity parameter
k	thermal conductivity ($\text{Wm}^{-1}\text{K}^{-1}$)
k_0	permiability of porous medium (m^2)
k_b	absorption parameter
L	reference length (m)
Nu_x	Nusselt number
Q	non-dimensional heat generation/absorption parameter
Q_0	heat generation/absorption parameter ($\text{Jm}^{-3}\text{K}^{-1}\text{s}^{-1}$)
q_w	heat flux at the surface of the cone (Wm^{-2})
r	radius of the cone
Rd	non-dimensional thermal radiation
Ri	Richardson number
T	temperature (K)
t	time (s)
Pr	Prandtl number

Greek letters

α	fractional order
β_T	volumetric thermal expansion (K^{-1})
Δt	time step
Δx	grid size in x direction
Δy	grid size in y direction
λ	relaxation time (s)
μ	dynamic viscosity ($\text{kgm}^{-1}\text{s}^{-1}$)
ν	kinematic viscosity (m^2s^{-1})
ρ	density (kgm^{-3})
σ	electrical conductivity (Sm^{-1})
σ_b	Stefan Boltzman coefficient ($\text{Wm}^{-2}\text{K}^{-4}$)
φ	nanoparticles volume fraction

Subscripts/Superscripts

*	non-dimensional
f	base fluid
hnf	hybrid nanofluid
i	grid point in x direction
j	grid point in y direction
k	time level
nf	nanofluid
p	nanoparticles

CONTACT Hanifa Hanif  hanifahani@outlook.com  Department of Mathematics, Sardar Bahadur Khan Women's University, Quetta, Pakistan; Department of Mathematical Sciences, Faculty of Science, Universiti Teknologi Malaysia, Johor Bahru, Johor 81310, Malaysia

© 2023 The Author(s). Published by Informa UK Limited, trading as Taylor & Francis Group.

This is an Open Access article distributed under the terms of the Creative Commons Attribution-NonCommercial License (<http://creativecommons.org/licenses/by-nc/4.0/>), which permits unrestricted non-commercial use, distribution, and reproduction in any medium, provided the original work is properly cited. The terms on which this article has been published allow the posting of the Accepted Manuscript in a repository by the author(s) or with their consent.

1. Introduction

Viscoelastic fluids are essential in every aspect of our lives. The Maxwell model is a classical model used to describe the viscoelastic behavior of materials, such as polymers and fluids, by combining a spring and a dashpot in series. The spring represents the elastic behavior of the material, while the dashpot represents the viscous behavior. In the Maxwell model, the spring and dashpot are both assumed to be characterized by a single relaxation time. Several studies have examined the behavior of Maxwell fluid in various contexts; just a few will be described here. The procedure of flooding the leftover oil in the dead end with viscoelastic fluid was studied by [1]. In this work, the conventional momentum equation is solved by using the fractional-order Maxwell. Additionally, the flow control equation for fractional-order viscoelastic fluids is given a semi-analytical solution. The findings demonstrate that velocity fractional-order derivative considerably influences the properties of polymer solutions and the fluid elasticity can significantly boost the effectiveness of oil repellency. Hanif [2,3] applied the Friedrich shear stress and Cattaneo heat flow model to the traditional upper convected Maxwell fluid model to account for nonlinear convection effects. The governing equations of the fractional Maxwell fluid are then solved under steady-state conditions, and the results are presented graphically and described in detail. According to the results of the study, the skin friction increases with an increase in the velocity relaxation time parameter, but the opposite effect is observed for the velocity fractional derivative parameter. This suggests that the fractional derivative parameter has a more significant effect on the flow behavior than the relaxation time parameter in this particular system. Ramesh et al. [4] three-dimensional flow of Maxwell nanofluid in a porous region limited by a bidirectional stretched sheet with non-linear thermal radiation and a heat source/sink. Convective conditions are established for temperature and nanoparticle concentration. It is mentioned that Brownian motion plays an important influence on temperature and heat transmission rate, and when the Deborah number increases, the concentration of nanoparticles and temperature drop. Ramesh and Gireesha [5] studied Maxwell fluid over a stretching sheet with convective boundary conditions in the presence of heat generation/absorption. Wang et al. [6] studied a generalized Maxwell fluid model of helical flow between two irrational coaxial circular cylinders. Cui et al. [7] investigated the petrophysical model for a field seismic survey. It was discovered that there are considerable differences in the characteristics of wave field propagation between regular wave equations and elastic wave equations in porous. The obtained results are useful to other related fields, such as seismic exploration of dense oil reservoirs, and micro seismic simulation in cracked reservoirs filled with fracturing fluid. Parvin et al. [8] presented a

2D-double diffusive layer flow model of Maxwell fluid in the presence of a magnetic field. Ferrás et al. [9] presented an interesting work by using distributed-order derivatives to develop a generalized viscoelastic model. In the paper referenced by [10], the authors used the Helmholtz eigenvalue problem and Laplace transforms to analytically solve the linear momentum and Poisson-Boltzmann equations in tandem in a triangular region to study the unsteady electroosmotic flow of generalized Maxwell fluid. The momentum equation using the fractional Maxwell model is formulated to evaluate unsteady stagnation-point flow based on the properties of pressure in the boundary layer by Bai et al. [11]. The newly designed finite difference scheme and L1 algorithm are used to solve the nonlinear fractional differential equations, and the convergence of the system is confirmed by creating a numerical example. Maxwell fluid performs the fastest slip transport under the isothermal condition, this was discussed by Anwar et al. [12]. They considered Caputo-Fabrizio and Atangana-Baleanu fractional derivatives to describe slip flow, shear stress, and heat transfer processes. To predict solutions of the momentum and heat equations in primary coordinates, the Laplace transformation is first applied to dimensionless fractional models and then Stehfest's numerical approach is used. Furthermore, the Laplace inversion algorithms developed by Durbin and Zakian serve to validate the computed solutions for the velocity and energy fields. Moosavi et al. [13] used the Maxwell fractional model to analyze viscoelastic non-Newtonian fluid natural convection heat flow on a vertical forward-facing step.

There are numerous industrial and engineering processes where the heat transfer phenomenon occurs. According to this framework, the most active topic of research in the scientific community is to increase the thermal performance of a system. In this context, nanofluids play a significant role and are used by engineers and scientists in different circumstances. For instance, Nimmy et al. [14] studied convection-radiation heat transfer of a partially wetted dovetail extended surface. Hanif and Shafie [15,16] investigated fractional Maxwell nanofluid flow over a horizontal surface and found that the nanoparticle volume fraction and conjugate parameter play an important role in enhancing the thermal efficiency of a system. The thermal performance of a constant hydromagnetic flow of $Ti_6Al_4V - H_2O$ nanofluid within two arbitrarily electrically conducting walls enclosing a Darcy-Brinkman porous medium under the effects of energy dissipation is explored by Singh et al. [17]. In the context of the Riga wedge, the flow of a mono nanofluid (SiO_2 /Kerosene oil) and hybrid nanofluid ($TiO_2 + SiO_2$ /Kerosene oil) is investigated by [18]. A heat transfer fractional Maxwell fluid along convective derivative oblique stagnation-point flow towards an oscillating tensile plate was observed by Bai et al. [19]. It is found that pressure

encourages Maxwell fluid velocity. Kaleem et al. [20] considered Maxwell hybrid nanofluid flow over an infinite vertical surface using the Caputo time fractional model. The impact of velocity slip and radiative heat on the thin-film flow of time-dependent hydrodynamic Oldroyd-B and Maxwell nanofluids is investigated by Minnam Reddy et al. [21]. The flow of fluid embedded in porous media with engine oil as the base fluid and nanoparticles of molybdenum disulfide (MoS₂) and zinc oxide (ZnO) is presented by Sagheer et al. [22]. With the help of the MATLAB bvp4c method, the rebuilt mathematical model is simulated using the local non-similarity technique up to the second level of truncation. Vijatha and Reddy [23] studied Maxwell hybrid nanofluid on a cylinder in the presence of non-linear thermal radiation and Cattaneo-Christov heat flux. Ramesh et al. [24] has shown how thermophoretic particle deposition and heat generation/absorption affect the laminar flow of a Casson hybrid-type nanofluid via a nonlinear stretched surface. Khan et al. [25] presented a role of partial slip and temperature-dependent viscosity in the bioconvection assessment of Maxwell nanofluid confined by a stretched. The major impacts of Friedrich shear stress, Cattaneo heat flux, and hybrid nanoparticles on the heat transfer and flow properties of Maxwell hybrid nanofluid is investigated by Hanif and Shafie [26] in the presence of magnetic field and Ohmic heating. The numerical solutions for the fractional Maxwell model are successfully provided using an implicit finite difference technique with the Caputo fractional derivative. Madhukesh et al. [27] investigated the heat transfer in MHD Casson–Maxwell nanofluid between two porous disks with Cattaneo–Christov. Ramesh et al. [28] investigated the chemical reaction and activation energy effects in Maxwell nanofluid flow.

Motivated by the above discussion, this research is designed to evaluate the thermal performance of Maxwell hybrid nanofluid in the presence of Newtonian heating. Prior research has not yet investigated the flow of a Maxwell hybrid nanofluid past a permeable cone. To bridge this research gap, this study article analyzes the flow of Maxwell hybrid nanofluid under the effects of heat radiation, heat generation/absorption, and Newtonian heating. Moreover, a fractional model might describe the complicated properties of viscoelastic material simply and elegantly. For instance, the exponential relaxation module of traditional ordinary models cannot accurately describe the algebraic degradation that many materials experience throughout the relaxation process. Therefore, a fractional Maxwell model has been suggested. A finite difference method, namely, the Crank-Nicolson method is explored to get the linear discrete forms of non-dimensional systems. After that, the numerical solutions are obtained by implementing the Thomas algorithm in MATLAB software. The obtained numerical results are presented via graphs and tables.

2. Mathematical formulation

The detailed mathematical modeling of the Maxwell hybrid nanofluid with time-fractional derivative is the emphasis of this section.

2.1. Stress tensor

The extra stress tensor τ for Maxwell fluid is described mathematically as

$$(\tau + \lambda^\alpha \partial_t^\alpha \tau) = \mu \dot{\gamma}, \tag{1}$$

where $\dot{\gamma}$ represents shear stress, λ is time relaxation, μ is the viscosity of the fluid. The well-known Caputo derivative ∂_t^α is defined as

$$\begin{aligned} \partial_t^\alpha f(t) &= \frac{\partial^\alpha}{\partial t^\alpha} f(t) \\ &= \frac{1}{\Gamma(n-\alpha)} \int_0^t (t-\tau)^{n-\alpha-1} \frac{\partial^n}{\partial \tau^n} f(\tau) d\tau, \\ n-1 &< \alpha < n, \quad n \in \mathbf{N}. \end{aligned} \tag{2}$$

The Gamma function $\Gamma(\cdot)$ is

$$\Gamma(\xi) = \int_R \tau^{\xi-1} e^{-\tau} d\tau, \quad \forall \xi \in \mathbf{C}, \Re(\xi) > 0. \tag{3}$$

2.2. Hybrid nanofluid properties

Let us add two distinct nanoparticles p_1, p_2 of volume fraction φ_{p_1} and φ_{p_1} , respectively, in a water-based fluid. Then the thermal physical properties of the resultant fluid, i.e. hybrid nanofluid are modified as [30–32]

$$\begin{aligned} \rho_{hnf} &= (1 - \varphi_{p_2})\rho_{nf} + \varphi_{p_2}\rho_{p_2}, \\ \rho_{nf} &= (1 - \varphi_{p_1})\rho_f + \varphi_{p_1}\rho_{p_1}, \\ \mu_{hnf} &= \frac{\mu_{nf}}{(1 - \varphi_{p_2})^{2.5}}, \quad \mu_{nf} = \frac{\mu_f}{(1 - \varphi_{p_1})^{2.5}}, \\ (\rho\beta_T)_{hnf} &= (1 - \varphi_{p_2})(\rho\beta_T)_{nf} + \varphi_{p_2}(\rho\beta_T)_{p_2}, \\ (\rho\beta_T)_{nf} &= (1 - \varphi_{p_1})(\rho\beta_T)_f + \varphi_{p_1}(\rho\beta_T)_{p_1}, \\ (\rho C_p)_{hnf} &= (1 - \varphi_{p_2})(\rho C_p)_{nf} + \varphi_{p_2}(\rho C_p)_{p_2}, \\ (\rho C_p)_{nf} &= (1 - \varphi_{p_1})(\rho C_p)_f + \varphi_{p_1}(\rho C_p)_{p_1}, \\ \frac{k_{hnf}}{k_{nf}} &= \frac{(k_{p_2} + 2k_{nf}) + 2\varphi_{p_2}(k_{p_2} - k_{nf})}{(k_{p_2} + 2k_{nf}) - \varphi_{p_2}(k_{p_2} - k_{nf})}, \\ \frac{k_{nf}}{k_f} &= \frac{(k_{p_1} + 2k_f) + 2\varphi_{p_1}(k_{p_1} - k_f)}{(k_{p_1} + 2k_f) - \varphi_{p_1}(k_{p_1} - k_f)}. \end{aligned} \tag{4}$$

2.3. Problem description

In this study, we consider that an incompressible Maxwell hybrid nanofluid ($\rho = constant$) is moving along a vertical cone. Two distinct nanoparticles, namely, Fe₃O₄ and Cu are suspended in the base fluid, their properties are given in Table 1. The surface of the cone is taken as the x-axis and the y-axis is considered normal to the cone, see Figure 1. Moreover, the

Table 1. Thermo-physical properties of water nanoparticles [29,30].

Materials	ρ kgm ⁻³	σ Sm ⁻¹	β_T K ⁻¹	C_p J(kgK) ⁻¹	k W(mK) ⁻¹
Pure water	997.1	0.05	21×10^{-5}	4179	0.613
Fe ₃ O ₄	5200	2.5×10^4	1.3×10^{-5}	670	6
Cu	8933	5.96×10^7	1.67×10^{-5}	385	401

viscous dissipation effects are supposed to be insignificant and no pressure gradient is applied. Bearing the above assumptions in mind, the boundary layer and Boussinesq approximations yield us to [33]

$$\frac{\partial}{\partial x}(ru) + \frac{\partial}{\partial y}(rv) = 0, \quad (5)$$

$$\begin{aligned} \rho_{hnf} \left(\frac{\partial u}{\partial t} + u \frac{\partial u}{\partial x} + v \frac{\partial u}{\partial y} \right) \\ = \frac{\partial \tau_{xy}}{\partial y} - \frac{\mu_{hnf}}{k_0} u \\ + g(\rho\beta_T)_{hnf} (T - T_\infty) \cos \beta, \end{aligned} \quad (6)$$

$$\begin{aligned} (\rho C_p)_{hnf} \left(\frac{\partial T}{\partial t} + u \frac{\partial T}{\partial x} + v \frac{\partial T}{\partial y} \right) \\ = k_{hnf} \frac{\partial^2 T}{\partial y^2} - \frac{\partial q_r}{\partial y} + Q_0(T - T_\infty), \end{aligned} \quad (7)$$

where $k_0, g, q_r, Q_0, \rho_{hnf}, \mu_{hnf}, (\rho\beta_T)_{hnf}, (\rho C_p)_{hnf},$ and k_{hnf} are permeability of porous medium, gravitational acceleration, radiative heat flux, heat generation/absorption, density, dynamic viscosity, thermal expansion, heat capacitance, and thermal conductivity of hybrid nanofluid, respectively. The imposed initial boundary conditions [34]

$$u = 0, \quad v = 0, \quad T = T_\infty, \quad t \leq 0, \quad \forall x, y,$$

$$u = 0, \quad v = 0, \quad T = T_\infty, \quad t > 0, \quad x = 0, \quad \forall y,$$

$$u = u_w, \quad \frac{\partial T}{\partial y} = -h_s T, \quad t > 0, \quad x > 0, \quad y = 0,$$

$$u = 0, \quad T = T_\infty, \quad t > 0, \quad \forall x, y \rightarrow \infty. \quad (8)$$

It is simple to anticipate that Equation (1) provides us

$$(1 + \lambda^\alpha \partial_t^\alpha) \tau_{xy} = \mu \frac{\partial u}{\partial y}. \quad (9)$$

Evaluating shear stress τ_{xy} from Equations (6) and (9) leads us to

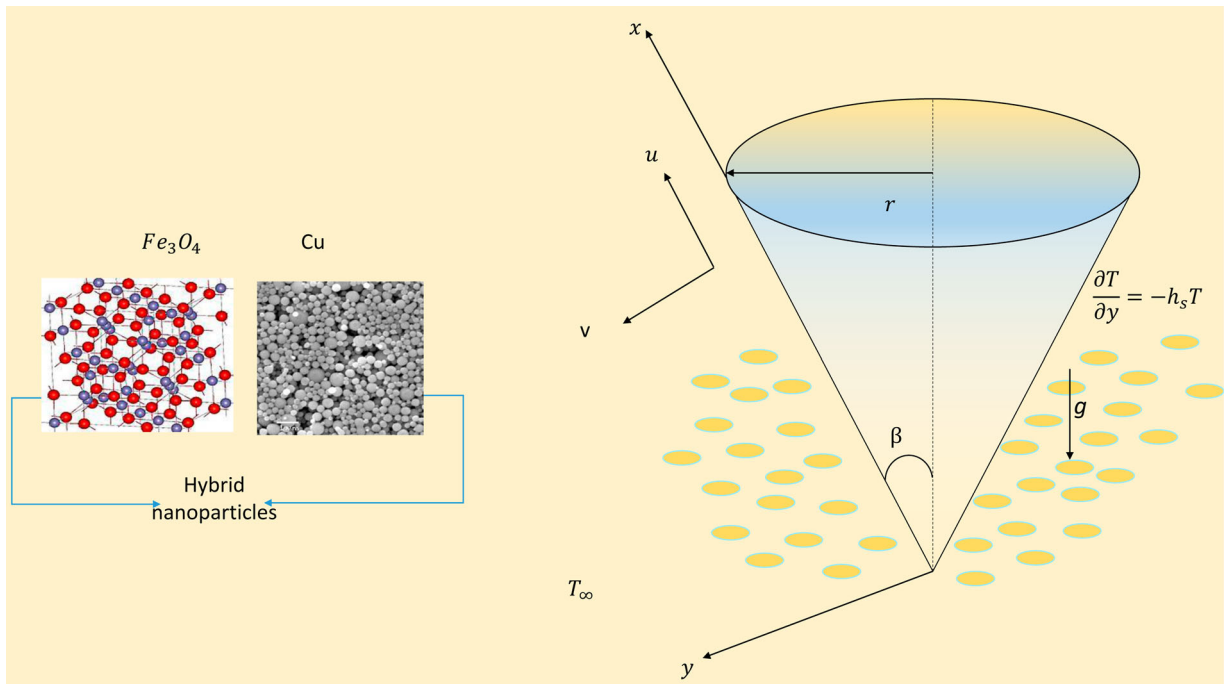
$$\begin{aligned} \rho_{hnf} (1 + \lambda^\alpha \partial_t^\alpha) \left(\frac{\partial u}{\partial t} + u \frac{\partial u}{\partial x} + v \frac{\partial u}{\partial y} \right) \\ = \mu_{hnf} \frac{\partial^2 u}{\partial y^2} - \frac{\mu_{hnf}}{k_0} (1 + \lambda^\alpha \partial_t^\alpha) u \\ + g(\rho\beta_T)_{hnf} (1 + \lambda^\alpha \partial_t^\alpha) (T - T_\infty) \cos \beta, \end{aligned} \quad (10)$$

Let us define the Rosseland approximation of the radiative heat flux q_r :

$$q_r = -\frac{4\sigma_b}{k_b} \frac{\partial T^4}{\partial y}, \quad (11)$$

here σ_b and k_b denote the Stefan–Boltzmann coefficient and absorption coefficient, respectively. The Taylor expansion of T^4 about T_∞ is

$$T^4 \cong T_\infty^4 + 4T_\infty^3 (T - T_\infty) + \dots \quad (12)$$

**Figure 1.** Graphical representation.

Using approximation (12) in Equation (11) and differentiating w.r.t “y” leads us to

$$\frac{\partial q_r}{\partial y} = -\frac{16\sigma_b T_\infty^3}{3k_b} \frac{\partial^2 T}{\partial y^2}. \quad (13)$$

The energy Equation (7) with thermal radiation (13) is given as

$$(\rho C_p)_{hnf} \left(\frac{\partial T}{\partial t} + u \frac{\partial T}{\partial x} + v \frac{\partial T}{\partial y} \right) = \left(k_{hnf} + \frac{16\sigma_b T_\infty^3}{3k_b} \right) \frac{\partial^2 T}{\partial y^2} + Q_0 (T - T_\infty). \quad (14)$$

2.4. Non-dimensional problem

To completely comprehend the mechanics of flow, we require a non-dimensional version of our suggested model. Therefore, we will introduce a set of non-dimensional parameters [35]:

$$\begin{aligned} x^* &= \frac{x}{L}, & y^* &= y \left(\frac{u_w}{v_f L} \right)^{\frac{1}{2}}, & r^* &= \frac{r}{L}, & t^* &= \frac{u_w t}{L}, \\ u^* &= \frac{u}{u_w}, & v^* &= v \left(\frac{u_w v_f}{L} \right)^{-\frac{1}{2}}, & T^* &= \frac{T - T_\infty}{T_\infty}, \\ \lambda^* &= \frac{u_w \lambda}{L}. \end{aligned} \quad (15)$$

Finally, we arrived at

$$\frac{\partial}{\partial x} (ru) + \frac{\partial}{\partial y} (rv) = 0, \quad (16)$$

$$\begin{aligned} C_1 (1 + \lambda^\alpha \partial_t^\alpha) \left(\frac{\partial u}{\partial t} + u \frac{\partial u}{\partial x} + v \frac{\partial u}{\partial y} \right) &= C_2 \frac{\partial^2 u}{\partial y^2} + \frac{C_2}{K} (1 + \lambda^\alpha \partial_t^\alpha) u \\ &+ C_3 Ri \cos \beta (1 + \lambda^\alpha \partial_t^\alpha) T, \end{aligned} \quad (17)$$

$$C_4 \left(\frac{\partial T}{\partial t} + u \frac{\partial T}{\partial x} + v \frac{\partial T}{\partial y} \right) = \frac{C_5 + Rd}{Pr} \frac{\partial^2 T}{\partial y^2} + QT. \quad (18)$$

Here Ri, Re, Gr, K, Pr, Rd, Q , and $C_1 - C_4$ are Richardson number, Reynolds number, Grashof number, porosity parameter, Prandtl number, radiation parameter, heat generation/absorption parameter, and nanofluid constants, respectively, defined as:

$$\begin{aligned} \frac{1}{K} &= \frac{v_f L}{u_w k_0}, & Ri &= \frac{Gr}{Re^2}, & Re &= \frac{u_w L}{v_f}, \\ Gr &= \frac{g \beta_T T_\infty L^3}{v_f^2}, & Pr &= \frac{(\mu C_p)_f}{k_f}, & Rd &= \frac{16\sigma_b T_\infty^3}{3k_b k_f}, \\ Q &= \frac{Q_0 L}{(\rho C_p)_f u_w}, & C_1 &= \frac{\rho_{hnf}}{\rho_f}, & C_2 &= \frac{\mu_{hnf}}{\mu_f}, \\ C_3 &= \frac{(\rho \beta_T)_{hnf}}{(\rho \beta_T)_f}, & C_4 &= \frac{(\rho C_p)_{hnf}}{(\rho C_p)_f}, & C_5 &= \frac{k_{hnf}}{k_f}. \end{aligned} \quad (19)$$

subject to initial boundary conditions:

$$u = 0, \quad v = 0, \quad T = 0, \quad t \leq 0, \quad \forall x, y,$$

$$\begin{aligned} u = 0, \quad v = 0, \quad T = 0, \quad t > 0, \quad x = 0, \quad \forall y, \\ u = 1, \quad \frac{\partial T}{\partial y} = -\gamma (1 + T), \quad t > 0, \quad x > 0, \quad y = 0, \\ u = 0, \quad T = 0, \quad t > 0, \quad \forall x, y \rightarrow \infty. \end{aligned} \quad (20)$$

2.5. Physical quantities

It is significant to discuss some important physical quantities like skin friction and Nusselt number [32]

$$C_f = \frac{\tau_w}{\rho_f u_w^2}, \quad Nu_x = \frac{x q_w}{k_f (T_w - T_\infty)}. \quad (21)$$

$\tau_w^* = \mu_{hnf} \left(\frac{\partial u}{\partial y} \right)_{y=0}$ and $q_w = -k_{hnf} \left(\frac{\partial T}{\partial y} \right)_{y=0}$. For a Maxwell fluid, the τ_w define by the following relationship:

$$(1 + \lambda^\alpha \partial_t^\alpha) \tau_w = \mu_{hnf} \left(\frac{\partial u}{\partial y} \right)_{y=0}. \quad (22)$$

Equation (15) helps us to obtained the non-dimensional form of Equation (21)

$$\begin{aligned} (1 + \lambda^\alpha \partial_t^\alpha) C_f Re^{1/2} &= C_2 \left(\frac{\partial u}{\partial y} \right)_{y=0}, & Nu_x Re^{-1/2} &= -C_5 x \left(\frac{\partial T}{\partial y} \right)_{y=0}. \end{aligned} \quad (23)$$

3. Numerical analysis

Assume the numerical solutions (u_{ij}^k, v_{ij}^k) at (x_i, y_j, t_k) with time step Δt and mesh size $(\Delta x, \Delta y)$ such that

$$\begin{cases} T_k = k \Delta t, & k = 0, 1, \dots, N \\ x_i = i \Delta x, & i = 1, 2, \dots, R, \\ y_j = j \Delta y, & j = 1, 2, \dots, S. \end{cases} \quad (24)$$

The L1 algorithm of the Caputo derivative is:

$$\begin{aligned} \frac{\partial^\alpha v}{\partial t^\alpha} &\simeq \frac{\Delta t^{-\alpha}}{2\Gamma(2-\alpha)} \\ &\left[v_{ij}^{k+1} + v_{ij}^k + \sum_{m=1}^k b_m v_{ij}^{k+1-m} + \sum_{m=1}^{k-1} b_m v_{ij}^{k-m} \right]. \end{aligned} \quad (25)$$

Note: $b_m = (a_m - a_{m-1})$, $a_m = (m+1)^{1-\alpha} - m^{1-\alpha}$. Let us define a set of constants

$$\begin{aligned} R_1 &= \lambda_1^\alpha \frac{\Delta t^{-\alpha}}{\Gamma(2-\alpha)}, & B_1 &= C_1 (1 + R_1), & B_2 &= C_1 R_1, \\ B_3 &= \frac{C_2}{K} (1 + R_1), & B_4 &= \frac{C_2}{K} R_1, \\ B_5 &= C_3 \cos \beta (1 + R_1), & B_6 &= C_3 \cos \beta R_1. \end{aligned} \quad (26)$$

Utilizing the approximation (25), constants (26) and the Crank-Nicolson method in Equations (18)–(16) lead us to:

$$\frac{u_{ij-1}^{k+1} - u_{i-1,j-1}^{k+1} + u_{ij}^{k+1} - u_{i-1,j}^{k+1} + u_{ij-1}^k - u_{i-1,j-1}^k + u_{ij}^k - u_{i-1,j}^k}{4\Delta x}$$

$$\begin{aligned}
 & + \frac{v_{ij}^{k+1} - v_{ij-1}^{k+1} + v_{ij}^k - v_{ij-1}^k}{2\Delta y} = 0. \quad (27) \\
 & + v_{ij}^k \frac{u_{ij+1}^{k+1} - u_{ij-1}^{k+1} + u_{ij+1}^k - u_{ij-1}^k}{4\Delta y} \\
 & \mathcal{B}_1 \left[\frac{u_{ij}^{k+1} - u_{ij}^k}{\Delta t} + u_{ij}^k \frac{u_{ij}^{k+1} - u_{i-1j}^{k+1} + u_{ij}^k - u_{i-1j}^k}{2\Delta x} \right. \\
 & \left. + \mathcal{B}_2 \left[\sum_{m=1}^k b_m \left\{ \frac{u_{ij}^{k+1-m} - u_{ij}^{k-m}}{\Delta t} \right\} \right] \right]
 \end{aligned}$$

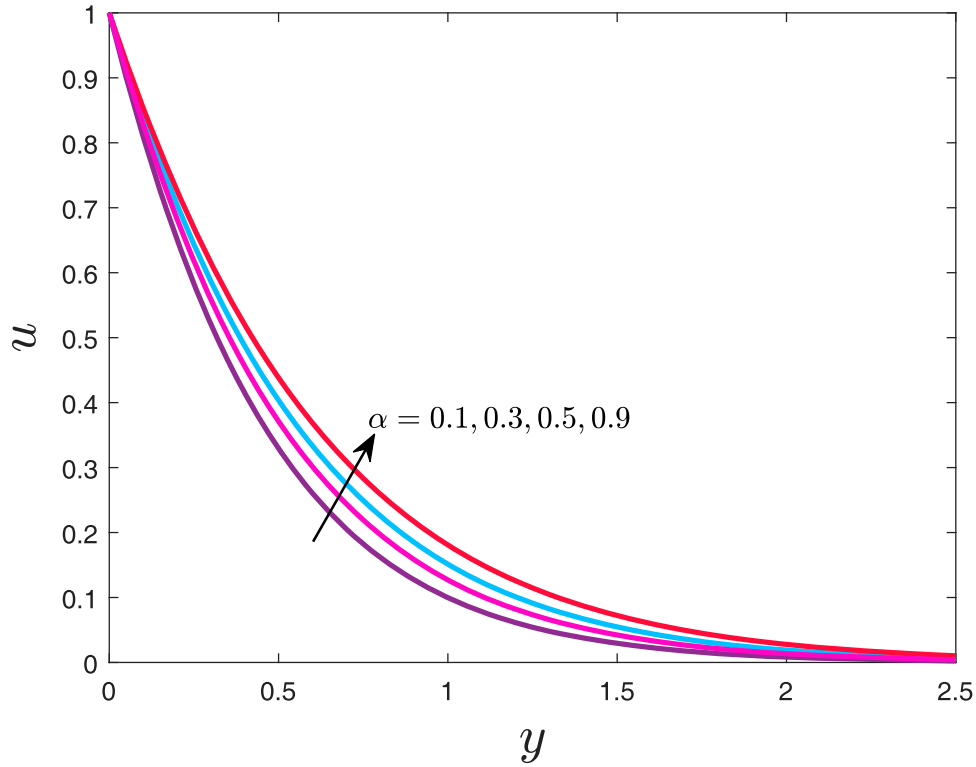


Figure 2. Velocity profile for α when $\lambda = 0.9, \varphi = 0.01, K = 0.5, Ri = 0.1, Rd = 0.3, Q = 0.1$, and $\gamma = 0.9$.

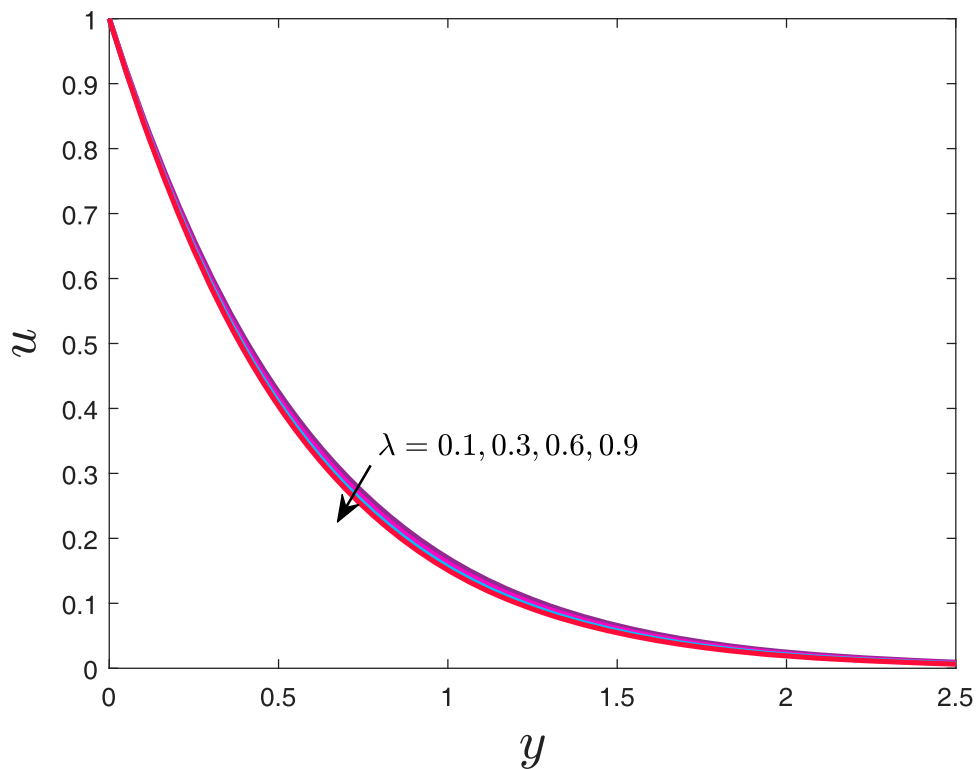


Figure 3. Velocity profile for λ when $\alpha = 0.5, \varphi = 0.01, K = 0.5, Ri = 0.1, Rd = 0.3, Q = 0.1$, and $\gamma = 0.9$.

$$\begin{aligned}
 & + u_{ij}^{k-m} \frac{u_{ij}^{k+1-m} - u_{i-1j}^{k+1-m}}{2\Delta x} \\
 & + v_{ij}^{k-m} \frac{u_{ij+1}^{k+1-m} - u_{ij-1}^{k+1-m}}{4\Delta y} \left. \right\} \\
 & + \sum_{m=1}^{k-1} b_m u_{ij}^{k-m} \left\{ \frac{u_{ij}^{k-m} - u_{i-1j}^{k-m}}{2\Delta x} \right. \\
 & \left. + v_{ij}^{k-m} \frac{u_{ij+1}^{k-m} - u_{ij-1}^{k-m}}{4\Delta y} \right\}
 \end{aligned}$$

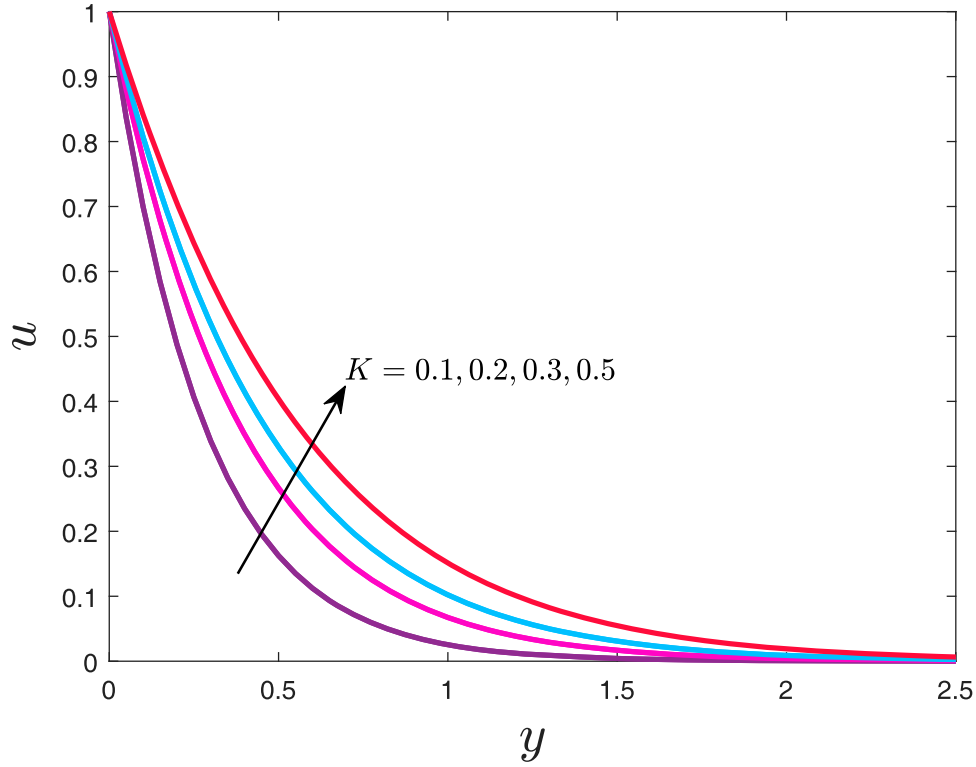


Figure 4. Velocity profile for K when $\alpha = 0.5, \lambda = 0.9, \varphi = 0.01, Ri = 0.1, Rd = 0.3, Q = 0.1,$ and $\gamma = 0.9$.

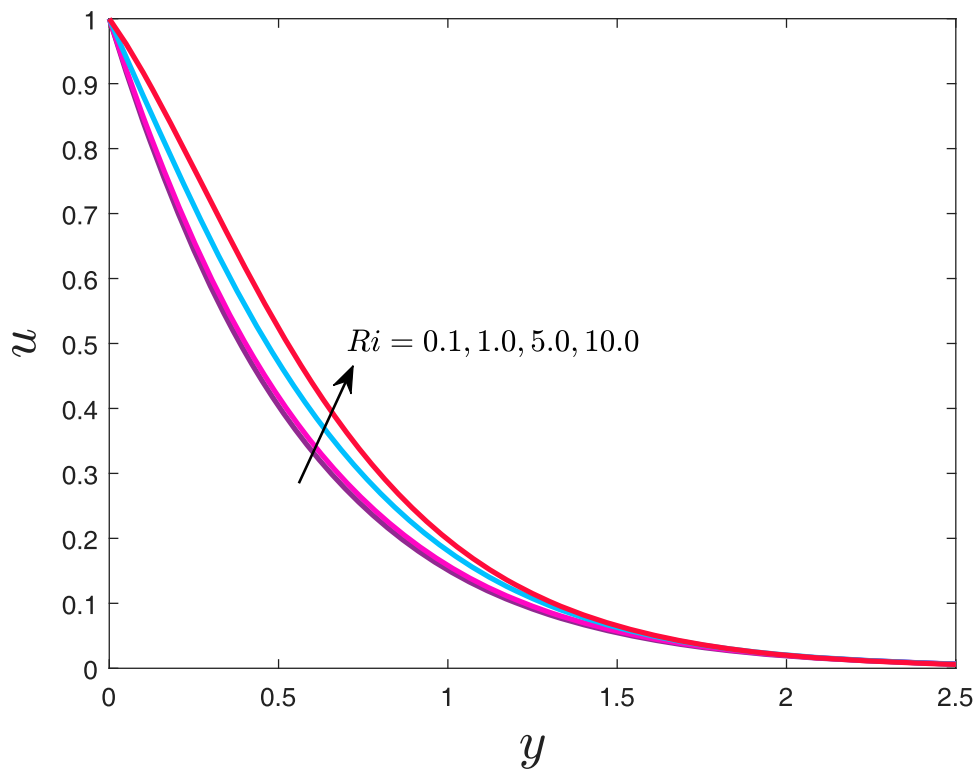


Figure 5. Velocity profile for Ri when $\alpha = 0.5, \lambda = 0.9, \varphi = 0.01, K = 0.5, Rd = 0.3, Q = 0.1,$ and $\gamma = 0.9$.

$$\begin{aligned}
 &= C_2 \frac{u_{ij+1}^{k+1} - 2u_{ij}^{k+1} + u_{ij-1}^{k+1} + u_{ij+1}^k - 2u_{ij}^k + u_{ij-1}^k}{2\Delta y^2} + \sum_{m=1}^{k-1} b_m u_{ij}^{k-m} \Bigg] + B_5 \frac{T_{ij}^{k+1} + T_{ij}^k}{2} \\
 &+ B_3 \frac{u_{ij}^{k+1} + u_{ij}^k}{2} + \frac{B_4}{2} \left[\sum_{m=1}^k b_m u_{ij}^{k+1-m} + \frac{B_6}{2} \left[\sum_{m=1}^k b_m T_{ij}^{k+1-m} + \sum_{m=1}^{k-1} b_m T_{ij}^{k-m} \right] \right]. \quad (28)
 \end{aligned}$$

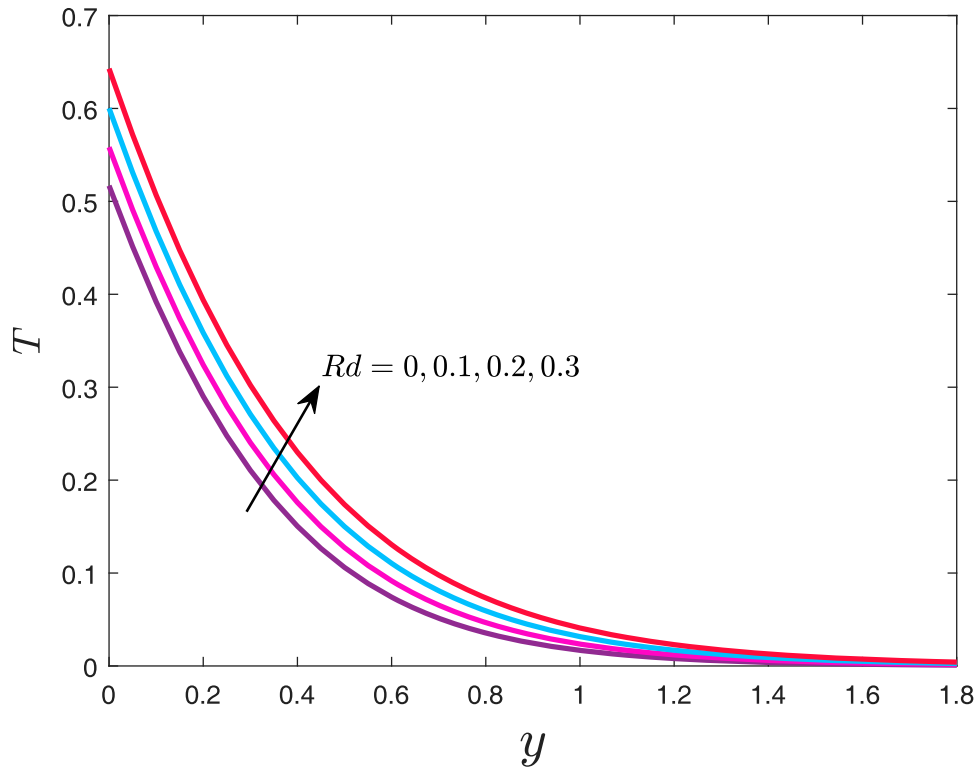


Figure 6. Temperature profile for Rd when $\alpha = 0.5, \lambda = 0.9, \varphi = 0.01, K = 0.5, Ri = 0.1, Q = 0.1$, and $\gamma = 0.9$.

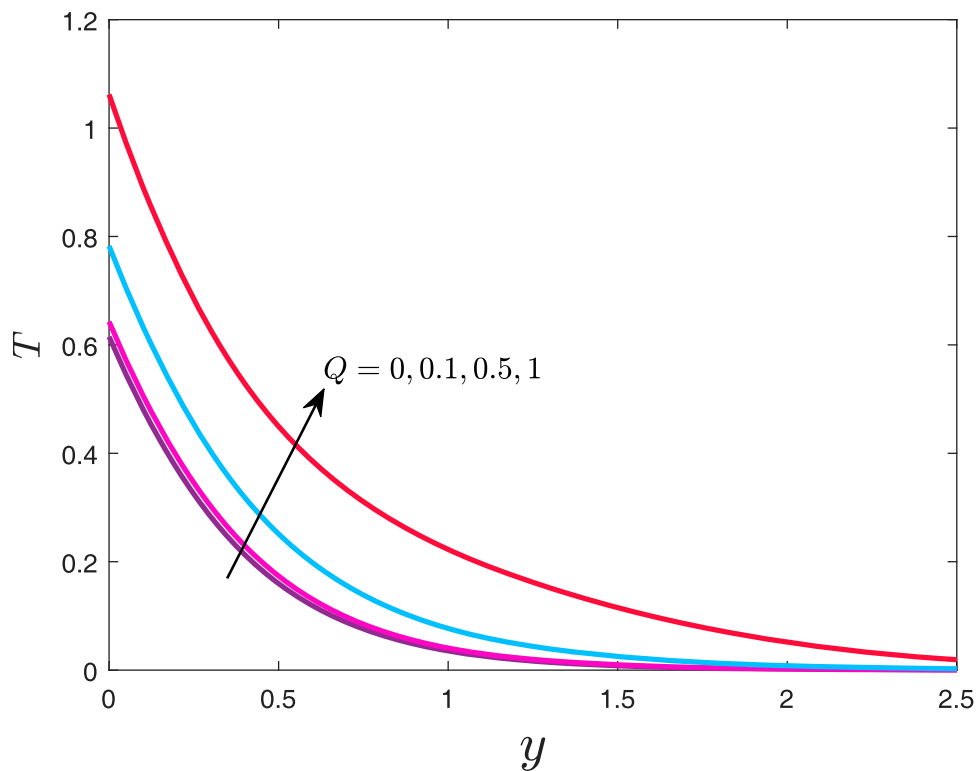


Figure 7. Temperature profile for Q when $\alpha = 0.5, \lambda = 0.9, \varphi = 0.01, K = 0.5, Ri = 0.1, Rd = 0.3$, and $\gamma = 0.9$.

$$\begin{aligned}
 & C_4 \left[\frac{T_{ij}^{k+1} - T_{ij}^k}{\Delta t} + u_{ij}^k \frac{T_{ij}^{k+1} - T_{i-1,j}^{k+1} + T_{ij}^k - T_{i-1,j}^k}{2\Delta x} \right. \\
 & \quad \left. + v_{ij}^k \frac{T_{ij+1}^{k+1} - T_{ij-1}^{k+1} + T_{ij+1}^k - T_{ij-1}^k}{4\Delta y} \right] \\
 & = \frac{C_5 + Rd}{Pr} \\
 & \quad \frac{T_{ij+1}^{k+1} - 2T_{ij}^{k+1} + T_{ij-1}^{k+1} + T_{ij+1}^k - 2T_{ij}^k + T_{ij-1}^k}{2\Delta y^2} \\
 & \quad + Q \frac{T_{ij}^{k+1} + T_{ij}^k}{2}. \tag{29}
 \end{aligned}$$

The limits of the rectangular domain are $x_{\max} = 1$ and $y_{\max} = 5$, where y_{\max} refers to $y \rightarrow \infty$. The time level Δt and mesh sizes $(\Delta x, \Delta y)$ along (x, y) direction are considered as $\Delta t = 0.001, \Delta x = 0.05$, and $\Delta y = 0.05$.

4. Results and discussion

In this research, Maxwell hybrid nanofluid flow over a cone enclosed in a porous media is investigated. In addition, the effects of thermal radiation, heat generation/absorption, and Newtonian boundary conditions are considered. The velocity, temperature, Nusselt number, and skin friction have been analyzed for the range of governing parameters: $0.1 \leq \alpha \leq 0.9, 0.1 \leq \lambda \leq 0.9, 0.1 \leq K \leq 0.5, 0 \leq Rd \leq 0.3, 0 \leq Q \leq 1$, and $0.1 \leq \gamma \leq 0.9$. The Nusselt number and skin friction of fluid flow over a cone with no slip velocity

Table 2. Comparison of nusselt number ($Nu_x Re^{-1/2}$) and skin friction ($C_f Re^{1/2}$) with previously published work when $\phi_{hnf} = \lambda = 1/K = Rd = Q = 0$ and $Ri = 1$.

Pr	$Nu_x Re^{-1/2}$		$C_f Re^{1/2}$	
	Sambath [36]	Present	Sambath [36]	Present
0.01	0.0797	0.0797	1.3356	1.3557
0.1	0.2115	0.2111	1.0911	1.0943
1	0.5125	0.5126	0.7688	0.7680
10	1.0356	1.0343	0.4856	0.4859

and constant wall temperature are calculated and compared with those reported by [36]. It is revealed that the results are in great agreement, see Table 2.

In Figures 2–5, show the subjectivity of the fractional parameter, relaxation time parameter, porosity parameter, and Richardson number on the velocity profile, respectively. It is discovered that the velocity increases for the increasing values of α in Figure 2. While in the case of relaxation time velocity decreases with the higher values of relaxation time parameter λ , see Figure 3. It was expected physically because the relaxation time corresponds to an increase in fluid viscoelasticity, a decrease in the velocity. It has been noted that the velocity increases for the increasing values of K , shown in Figure 4. In general, the permeability of the porous media or porosity indicates a medium’s ability to enable fluid to pass through it, and increasing the porosity parameter allows the fluid to move swiftly, resulting in increased velocity. The effects of Richardson number Ri on the velocity profile is drawn in Figure 5. This figure shows that the velocity

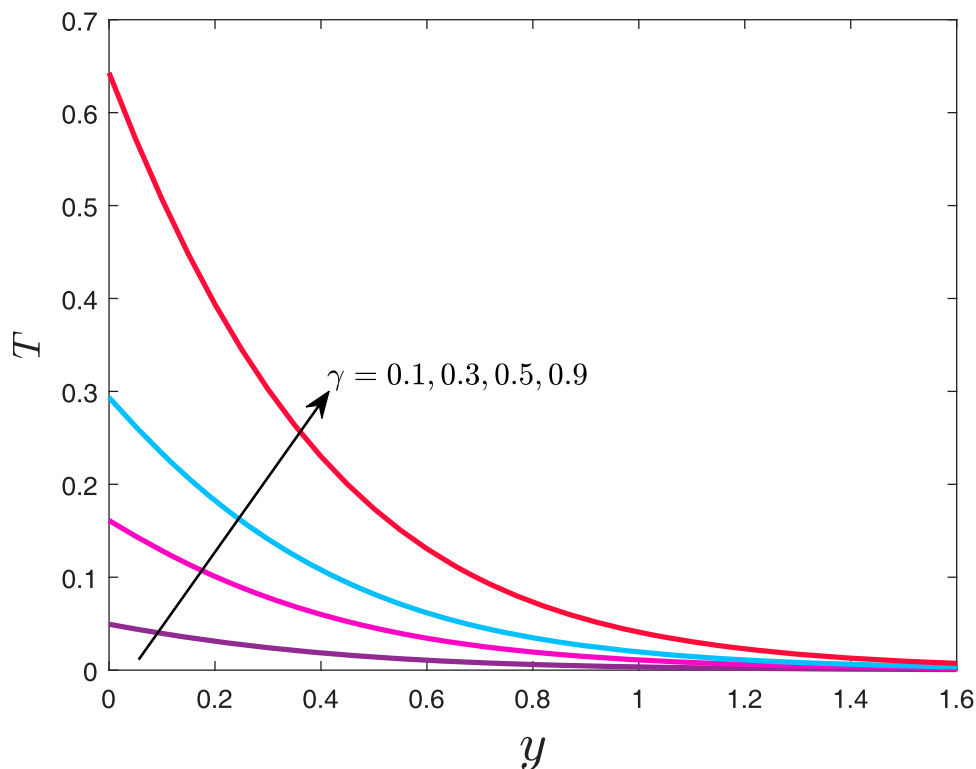


Figure 8. Temperature profile for γ when $\alpha = 0.5, \lambda = 0.9, \phi = 0.01, K = 0.5, Ri = 0.1, Rd = 0.3$, and $Q = 0.1$.

of the fluid increases against Ri . The Richardson number quantifies the influence of buoyancy in contrast to the inertia of the external force. For higher values of Ri , there is a favorable pressure gradient due to buoyancy forces, which causes the flow to accelerate. Figures 6–8 show the fluctuations in the temperature of Maxwell hybrid nanofluid caused by active governing parameters. The temperature profile for various values of radiation parameter Rd is plotted in Figure 6. The pattern of this graph illustrates how the temperature profile of the fluid increases with increasing assumptions of the radiation parameter Rd . Generally, increasing values of the radiation parameter promote radiative transmission of heat, which improves radiative flux; as a result, the temperature profile steadily rises as the value of

Rd increases. Figure 7 shows that the temperature of the fluid increases for increasing values of heat generation parameter Q . This is because the heat generation term is a source of thermal energy, and the temperature of the fluid is directly related to the amount of thermal energy present in the system. In Figure 8 temperature profile is drawn for the conjugate heat parameter. The temperature of the fluid is related to the conjugate heat parameter. Specifically, as the value of the conjugate heat parameter increases, the temperature of the fluid also increases. This is because the conjugate heat parameter represents the efficiency with which the fluid can dissipate thermal energy. When this parameter is high, the fluid can more effectively convert mechanical energy into thermal energy, which raises

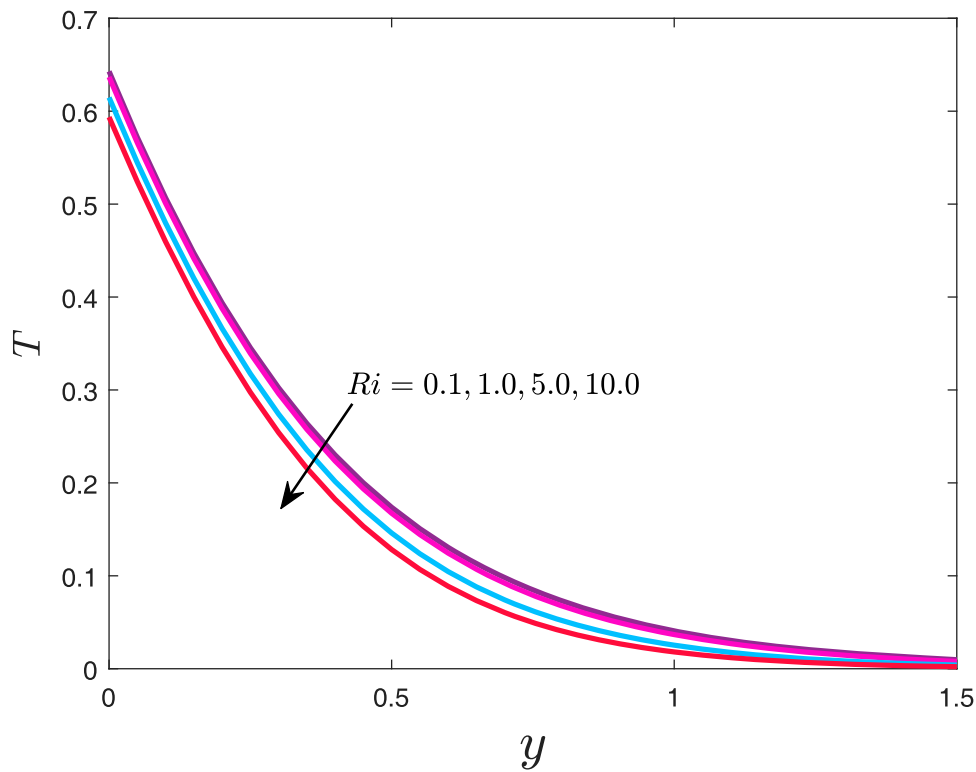


Figure 9. Temperature profile for Ri when $\alpha = 0.5, \lambda = 0.9, \varphi = 0.01, K = 0.5, Rd = 0.3, Q = 0.1$, and $\gamma = 0.9$.

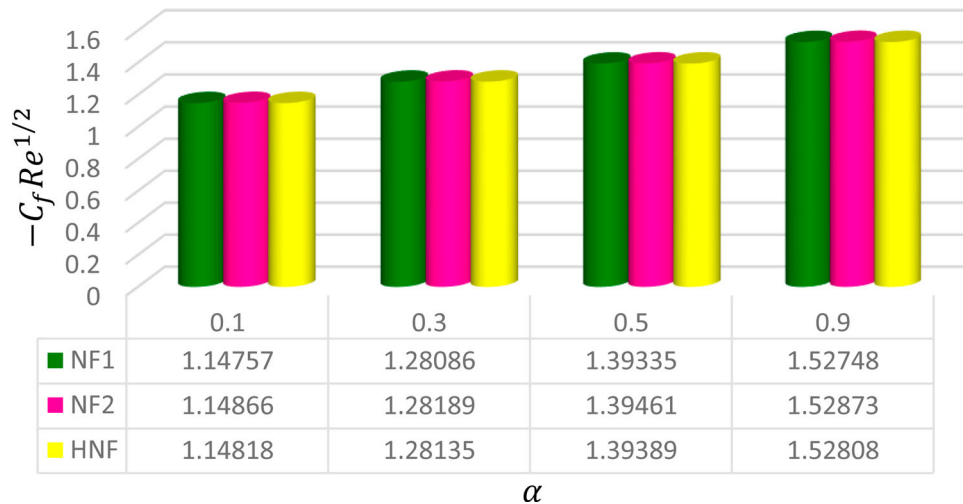


Figure 10. Skin friction for α when $\lambda = 0.9, \varphi = 0.01, K = 0.5, Ri = 0.1, Rd = 0.3, Q = 0.1$, and $\gamma = 0.9$.

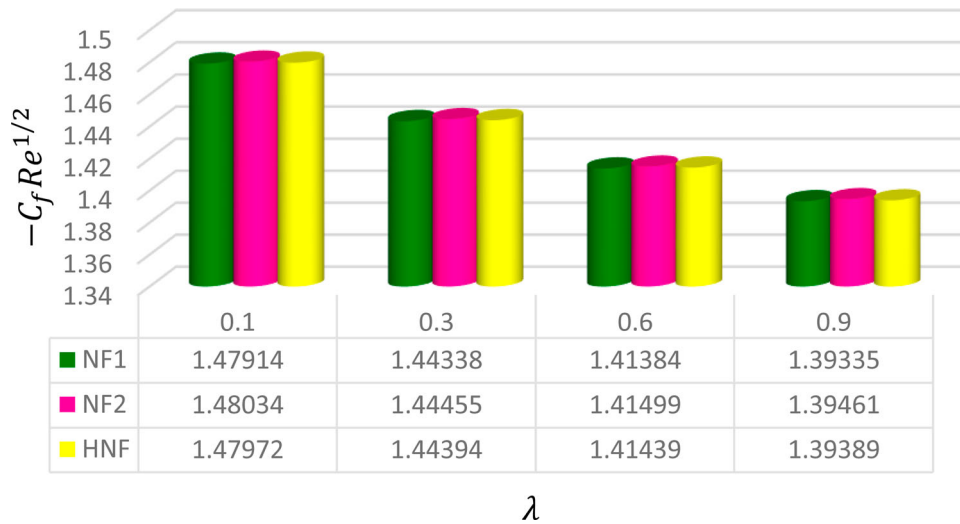


Figure 11. Skin friction for λ when $\alpha = 0.5, \varphi = 0.01, K = 0.5, Ri = 0.1, Rd = 0.3, Q = 0.1,$ and $\gamma = 0.9$.

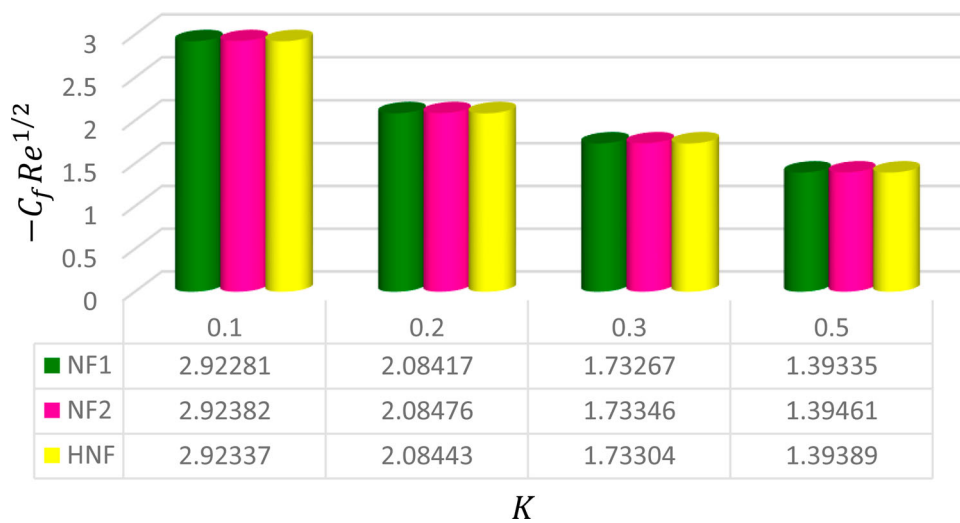


Figure 12. Skin friction for K when $\alpha = 0.5, \lambda = 0.9, \varphi = 0.01, Ri = 0.1, Rd = 0.3, Q = 0.1,$ and $\gamma = 0.9$.

the temperature of the fluid. The decreasing temperature profile against Richardson number is illustrated in Figure 9. Temperature distributions approach a linear decrease from the wall to the free stream with low Richardson numbers, which correlate to weak buoyant forces (low Grashof numbers). The profiles indicate monotonic deterioration at larger Ri values.

The numerical results for the skin friction of different nanofluids are depicted in Figures 10–12. The results show that the fractional parameter has a positive correlation with skin friction, see Figure 10. A remarkable change in skin friction due to the relaxation time parameter is noted in Figure 11, that when it increases the skin friction decreases. In Figure 12, an identical behavior is observed for increasing values of the porosity parameter. The behavior of the Nusselt number for different nanofluids is studied in Figures 13–16. Increasing values of nanoparticle concentration increase the Nusselt number as shown in Figure 13. It was predicted, because nanoparticles have a propensity to enhance the thermal conductivity of weak convective fluids, and therefore the Nusselt number or heat transfer rate of a system.

However, this trend is reversed for increasing values of radiation and heat generation parameters as shown in Figures 14 and 15. The reduced convective heat transmission is owing to the increased radiative heat transfer. The Nusselt number decreases because it measures the proportion of convective to conductive heat transfer. On the other hand, the conjugate parameter γ increases the heat transfer efficiency, see Figure 16. It is obvious because the Nusselt number is directly proportional to the temperature gradient at the wall which is in direct correlation with the conjugate heat parameter. For this reason, the Nusselt number grows when γ increases.

5. Conclusions

The boundary layer flow of a fractional Maxwell hybrid nanofluid with Newtonian heating is examined in the presence of a porous medium. The Crank–Nicolson technique and the L1 algorithm are utilized to generate numerical solutions for the suggested problem. The impacts of pertinent flow parameters on fluid velocity, heat transfer, wall shear stress, and Nusselt number are

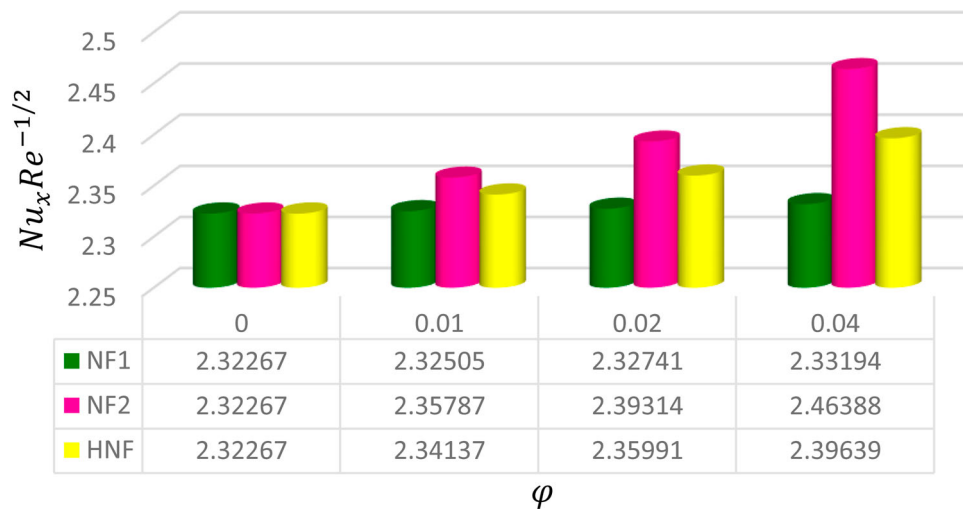


Figure 13. Nusselt number for ϕ when $\alpha = 0.5, \lambda = 0.9, K = 0.5, Ri = 0.1, Rd = 0.3, Q = 0.1$, and $\gamma = 0.9$.

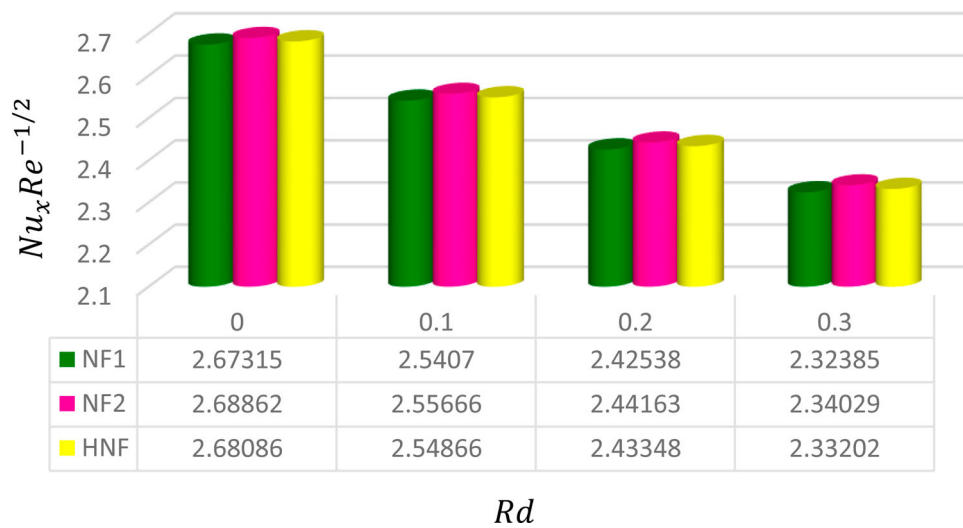


Figure 14. Nusselt number for Rd when $\alpha = 0.5, \lambda = 0.9, \phi = 0.01, K = 0.5, Ri = 0.1, Q = 0.1$, and $\gamma = 0.9$.

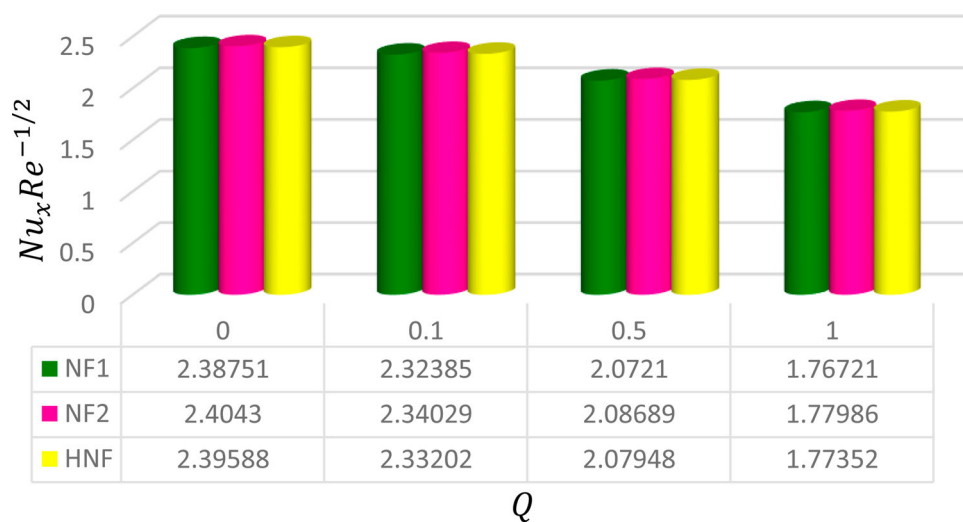


Figure 15. Nusselt number for Q when $\alpha = 0.5, \lambda = 0.9, \phi = 0.01, K = 0.5, Ri = 0.1, Rd = 0.3$, and $\gamma = 0.9$.

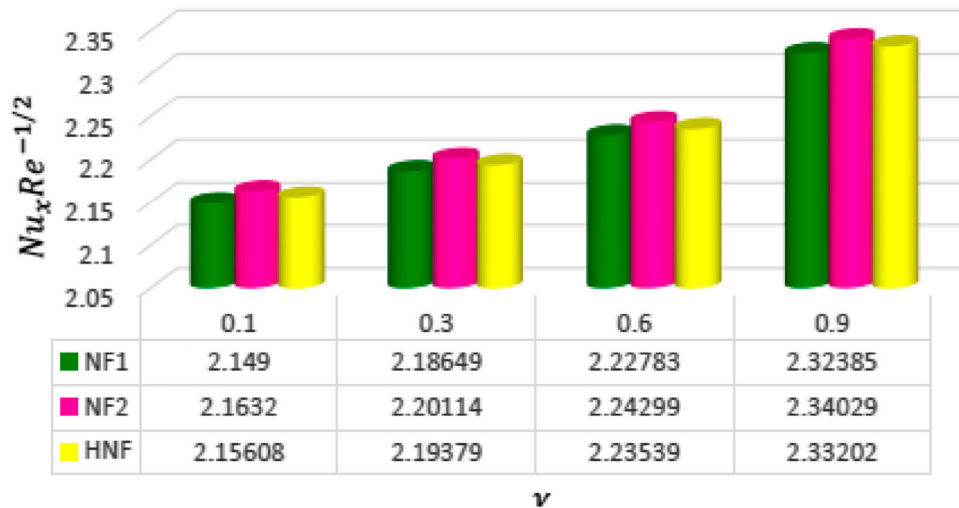


Figure 16. Nusselt number for γ when $\alpha = 0.5, \lambda = 0.9, \varphi = 0.01, K = 0.5, Ri = 0.1, Rd = 0.3,$ and $Q = 0.1$.

studied in a variety of illustrations. The major outcomes of the research are listed below:

- The thermal conductivity boosts as the φ increases and raises the heat transfer of the fluid by 3.1% at 4% vol. of Cu – Fe₃O₄ nanoparticles.
- The fluid motion slows down when λ rises, indicating that the viscoelasticity rises, and the fluid motion and wall shear stress both decrease.
- The temperature profiles indicate monotonic deterioration at larger Ri values.
- The results demonstrated that raising the Rd leads the thermal boundary layer to thicken and lower the Nusselt number.

Acknowledgements

The authors would like to acknowledge the financial support from Universiti Teknologi Malaysia for the funding under UTM Fundamental Research (UTMFR: Q.J130000.3854.23H22).

Disclosure statement

The authors wish to confirm that there are no known conflicts of interest associated with this publication.

ORCID

Hanifa Hanif  <http://orcid.org/0000-0003-0053-0653>

Sharidan Shafie  <http://orcid.org/0000-0001-7795-2278>

References

- [1] Huang J, Chen L, Li S, et al. Numerical study for the performance of viscoelastic fluids on displacing oil based on the fractional-order Maxwell model. *Polymers*. 2022;14:5381. doi:10.3390/polym14245381
- [2] Hanif H. Cattaneo–Friedrich and Crank–Nicolson analysis of upper-convected Maxwell fluid along a vertical plate. *Chaos Solitons Fractals*. 2021;153:Article ID 111463. doi:10.1016/j.chaos.2021.111463
- [3] Hanif H. A computational approach for boundary layer flow and heat transfer of fractional Maxwell fluid. *Math Comput Simul*. 2022;191:1–13. doi:10.1016/j.matcom.2021.07.024
- [4] Ramesh G, Prasannakumara B, Giresha B, et al. Three dimensional flow of Maxwell fluid with suspended nanoparticles past a bidirectional porous stretching surface with thermal radiation. *Therm Sci Eng Prog*. 2017;1:6–14. doi:10.1016/j.tsep.2017.02.006
- [5] Ramesh G, Giresha B. Influence of heat source/sink on a Maxwell fluid over a stretching surface with convective boundary condition in the presence of nanoparticles. *Ain Shams Eng J*. 2014;5:991–998. doi:10.1016/j.asej.2014.04.003
- [6] Wang P, Liu J-L, Wang F. The first solution for the helical flows of generalized Maxwell fluid with longitudinal time dependent shear stresses on the boundary. *Therm Sci*. 2022;26:1113–1121. doi:10.2298/TSCI2202113W
- [7] Cui Z-W, Liu J-X, Wang K-X. Elastic waves in non-newtonian (Maxwell) fluid-saturated porous media. *Waves Random Media*. 2003;13:191–203. doi:10.1088/0959-7174/13/3/304
- [8] Parvin S, Isa SSPM, Al-Duais FS, et al. The flow, thermal and mass properties of Soret-Dufour model of magnetized Maxwell nanofluid flow over a shrinkage inclined surface. *PLoS One*. 2022;17:Article ID e0267148. doi:10.1371/journal.pone.0267148
- [9] Ferrás LL, Morgado ML, Rebelo M. A generalised distributed-order Maxwell model. *Math Methods Appl Sci*. 2023;46:368–387. doi:10.1002/mma.8516
- [10] Akyildiz FT, Siginer DA. Exact solution of the startup electroosmotic flow of generalized Maxwell fluids in triangular microducts. *J Fluids Eng*. 2021;143. Article ID 101302. doi:10.1115/1.4050940
- [11] Bai Y, Huo L, Zhang Y. Unsteady stagnation-point flow and heat transfer of fractional Maxwell fluid towards a time dependent stretching plate with generalized Fourier's law. *Int J Numer Methods Heat Fluid Flow*. 2021;31:1345–1368. doi:10.1108/HFF-04-2020-0217
- [12] Anwar T, Kumam P, Khan I, et al. Thermal analysis of MHD convective slip transport of fractional Oldroyd-b fluid over a plate. *Mech Time-Depend Mater*. 2021;26:431–462. doi:10.1007/s11043-021-09495-z
- [13] Moosavi R, Moltafet R, Shekari Y. Analysis of viscoelastic non-Newtonian fluid over a vertical forward-facing step using the Maxwell fractional model. *Appl Math Comput*. 2021;401. doi:10.1016/j.amc.2021.126119

- [14] Nimmy P, Nagaraja K, Srilatha P, et al. Implication of radiation on the thermal behavior of a partially wetted dovetail fin using an artificial neural network. *Case Stud Therm Eng.* 2023;51:Article ID 103552. doi:10.1016/j.csite.2023.103552
- [15] Hanif H, Shafie S. Impact of Al_2O_3 in electrically conducting mineral oil-based Maxwell nanofluid: application to the petroleum industry. *Fractal Fract.* 2022;6:180. doi:10.3390/fractalfract6040180
- [16] Hanif H, Shafie S. Interaction of multi-walled carbon nanotubes in mineral oil based Maxwell nanofluid. *Sci Rep.* 2022;12:1–16. doi:10.1038/s41598-022-07958-y
- [17] Singh JK, Seth GS, Hussain SM. Thermal performance of hydromagnetic nanofluid flow within an asymmetric channel with arbitrarily conductive walls filled with Darcy-Brinkman porous medium. *J Magn Magn Mater.* 2023;582. Article ID 171034. doi:10.1016/j.jmmm.2023.171034
- [18] Yahya AU, Siddique I, Jarad F, et al. On the enhancement of thermal transport of kerosene oil mixed TiO_2 and SiO_2 across riga wedge. *Case Stud Therm Eng.* 2022;34. Article ID 102025. doi:10.1016/j.csite.2022.102025
- [19] Bai Y, Wang X, Zhang Y. Unsteady oblique stagnation-point flow and heat transfer of fractional Maxwell fluid with convective derivative under modified pressure field. *Comput Math Appl.* 2022;123:13–25. doi:10.1016/j.camwa.2022.07.013
- [20] Kaleem MM, Asjad MI, Usman M, et al. Effects of natural convection flow of fractional Maxwell hybrid nanofluid by finite difference method. *Waves Random Complex Media.* 2023;1–16. doi:10.1080/17455030.2022.2164381
- [21] Minnam Reddy VR, Girinath Reddy M, Dinesh P, et al. Radiative heat and slip effects on blood-based hydrodynamic film flow of Maxwell/Oldroyd-B cross nanofluids: a bioapplication. *Waves Random Complex Media.* 2022;1–18. doi:10.1080/17455030.2022.2163058
- [22] Sagheer S, Farooq U, Hussain M. Non-similar investigation of enhanced thermal efficiency of Maxwell based hybrid nanofluid ($MOS_2 + ZnO$) across a linearly stretched surface. *J Magn Magn Mater.* 2023;565:Article ID 170285. doi:10.1016/j.jmmm.2022.170285
- [23] Vijatha M, Reddy PBA. Entropy generation on MHD Maxwell hybrid nanofluid over a stretching cylinder with Cattaneo-Christov heat flux: analytical and numerical simulations. *Proc Inst Mech Eng Part C J Mech Eng Sci.* 2022;237(8):Article ID 09544062221128449. doi:10.1177/09544062221128449
- [24] Ramesh G, Madhukesh J, Khan U, et al. Inspection of hybrid nanoparticles flow across a nonlinear/linear stretching surface when heat sink/source and thermophoresis particle deposition impacts are significant. *Int J Mod Phys B.* 2023;37:Article ID 2350008. doi:10.1142/S021797922350008X
- [25] Khan SU, Usman, Al-Khaled K, et al. Implication of Arrhenius activation energy and temperature-dependent viscosity on non-Newtonian nanomaterial bio-convective flow with partial slip. *Arab J Sci Eng.* 2022;47:7559–7570. doi:10.1007/s13369-021-06274-3.
- [26] Hanif H, Shafie S. Application of Cattaneo heat flux to Maxwell hybrid nanofluid model: a numerical approach. *Eur Phys J Plus.* 2022;137:989. doi:10.1140/epjp/s13360-022-03209-1
- [27] Madhukesh JK, Ramesh GK, Shehzad SA, et al. Thermal transport of MHD Casson–Maxwell nanofluid between two porous disks with Cattaneo–Christov theory. *Numer Heat Transf A Appl.* 2023;1–16. doi:10.1080/10407782.2023.2214322
- [28] Ramesh G, Shehzad S, Hayat T, et al. Activation energy and chemical reaction in Maxwell magneto-nanofluid with passive control of nanoparticle volume fraction. *J Braz Soc Mech Sci Eng.* 2018;40:1–9. doi:10.1007/s40430-018-1353-8
- [29] Hanif H, Lund LA, Mahat R, et al. Heat transfer analysis of Maxwell hybrid nanofluid with fractional Cattaneo heat flux. *Alex Eng J.* 2023;72:545–557. doi:10.1016/j.aej.2023.04.022
- [30] Ali A, Bukhari Z, Amjad M, et al. Newtonian heating effect in pulsating magnetohydrodynamic nanofluid flow through a constricted channel: A numerical study. *Front Energy Res.* 2022;10:Article ID 1002672. doi:10.3389/fenrg.2022.1002672
- [31] Hanif H. A finite difference method to analyze heat and mass transfer in kerosene based γ -oxide nanofluid for cooling applications. *Phys Scr.* 2021;96:Article ID 095215. doi:10.1088/1402-4896/ac098a
- [32] Hussain SM, Khan U, Zaib A, et al. Numerical computation of mixed convective entropy optimized in Darcy-Forchheimer flow of cross nanofluids through a vertical flat plate with irregular heat source/sink. *Tribol Int.* 2023;187:Article ID 108757. doi:10.1016/j.triboint.2023.108757
- [33] Hanif H, Khan I, Shafie S. A novel study on time-dependent viscosity model of magneto-hybrid nanofluid flow over a permeable cone: applications in material engineering. *Eur Phys J Plus.* 2020;135:730. doi:10.1140/epjp/s13360-020-00724-x
- [34] Krishna MV. Chemical reaction, heat absorption and Newtonian heating on MHD free convective Casson hybrid nanofluids past an infinite oscillating vertical porous plate. *Int Commun Heat Mass Transf.* 2022;138: Article ID 106327. doi:10.1016/j.icheatmasstransfer.2022.106327
- [35] Hanif H, Jamshed W, Eid MR, et al. Numerical Crank-Nicolson methodology analysis for hybridity aluminium alloy nanofluid flowing based-water via stretchable horizontal plate with thermal resistive effect. *Case Stud Therm Eng.* 2023;42:Article ID 102707. doi:10.1016/j.csite.2023.102707
- [36] Sambath P, Pullepu B, Hussain T, et al. Radiated chemical reaction impacts on natural convective MHD mass transfer flow induced by a vertical cone. *Results Phys.* 2018;8:304–315. doi:10.1016/j.rinp.2017.12.005